

● *Original Contribution*

## EXPERIMENTAL APPLICATION OF ULTRAFAST IMAGING TO SPECTRAL TISSUE CHARACTERIZATION

JULIAN GARCIA-DUITAMA,<sup>\*†</sup> BORIS CHAYER,<sup>\*‡</sup> AIGUO HAN,<sup>†</sup> DAMIEN GARCIA,<sup>\*‡§</sup> MICHAEL L. OELZE,<sup>†</sup>  
and GUY CLOUTIER<sup>\*§</sup>

<sup>\*</sup>Laboratory of Biorheology and Medical Ultrasonics, University of Montreal Hospital Research Center (CRCHUM), Montreal, Quebec, Canada; <sup>†</sup>Bioacoustics Research Laboratory, Department of Electrical and Computer Engineering, University of Illinois at Urbana-Champaign, Urbana, Illinois, USA; <sup>‡</sup>Research Unit of Biomechanics and Imaging in Cardiology, CRCHUM, Montreal, Quebec, Canada; and <sup>§</sup>Department of Radiology, Radio-Oncology and Nuclear Medicine and Institute of Biomedical Engineering, University of Montreal, Montreal, Quebec, Canada

(Received 6 August 2014; revised 22 April 2015; in final form 26 April 2015)

**Abstract**—Ultrasound ultrafast imaging (UI) allows acquisition of thousands of frames per second with a sustained image quality at any depth in the field of view. Therefore, it would be ideally suited to obtain good statistical sampling of fast-moving tissues using spectral-based techniques to derive the backscatter coefficient (BSC) and associated quantitative parameters. In UI, an image is formed by insonifying the medium with plane waves steered at different angles, beamforming them and compounding the resulting radiofrequency images. We aimed at validating, experimentally, the effect of these beamforming protocols on the BSC, under both isotropic and anisotropic conditions. Using UI techniques with a linear array transducer (5–14 MHz), we estimated the BSCs of tissue-mimicking phantoms and flowing porcine blood at depths up to 35 mm with a frame rate reaching 514 Hz. UI-based data were compared with those obtained using single-element transducers and conventional focusing imaging. Results revealed that UI compounded images can produce valid estimates of BSCs and effective scatterer size (errors less than  $2.2 \pm 0.8$  and  $0.26 \pm 0.2$  dB for blood and phantom experiments, respectively). This work also describes the use of pre-compounded UI images (*i.e.*, steered images) to assess the angular dependency of circulating red blood cells. We have concluded that UI data sets can be used for BSC spectral tissue analysis and anisotropy characterization. (E-mail: [guy.cloutier@umontreal.ca](mailto:guy.cloutier@umontreal.ca)) © 2015 World Federation for Ultrasound in Medicine & Biology.

**Key Words:** Quantitative ultrasound, Backscatter coefficient, Spectral analysis, Plane wave imaging, Reference phantom technique, Planar reflector technique, Erythrocyte aggregation.

### INTRODUCTION

Ultrasound tissue characterization using spectral methods has been extensively studied and validated, both theoretically and experimentally, over the last 30 y (Faran 1951; Insana and Brown 1993; Lizzi et al. 1983, 1988; Waag et al. 1983). Its clinical relevance was reported in studies on detection of inflammatory response (Trippette et al. 2013), breast cancer treatment monitoring (Sadeghi-Naini et al. 2013), detection of prothrombotic factors (Yu et al. 2011) and prediction of coronary plaque composition (Nair et al. 2002).

The central quantitative parameter used for spectral tissue characterization is the backscatter coefficient (BSC). The BSC is a fundamental property of a tissue that describes how effectively it is able to return acoustic energy to the transducer, independent of the investigated depth and the instrumentation (Ghoshal et al. 2013; Wear et al. 2005). Formally, it is defined as the scattered intensity in the backward direction per unit solid angle per unit volume normalized by the incident wave intensity (Ghoshal et al. 2013). In practice, the BSC is related to the power spectral density (PSD) of the radiofrequency (RF) signal echo (Oelze 2013; Szabo 2004), as described by

$$\text{PSD}(f) = A(f, d)I(f, d)\text{BSC}(f), \quad (1)$$

where  $f$  is the insonifying frequency;  $A$  is the signal attenuation at depth  $d$  caused by absorption, scattering and

Address correspondence to: Guy Cloutier, Laboratory of Biorheology and Medical Ultrasonics, University of Montreal Hospital Research Center, 900 St-Denis, Viger Tower, Montreal, Quebec H2X 0A9, Canada. E-mail: [guy.cloutier@umontreal.ca](mailto:guy.cloutier@umontreal.ca)

transmission of ultrasound in the acoustic path; and  $I$  is the instrumentation effect that accounts for the transmitted pulse, transducer filtering and beam diffraction. With this simplified definition, estimation of the BSC is reduced to the compensation of two main confounding factors: instrumentation properties and tissue attenuation.

Among different strategies to compensate for the instrumentation, two techniques are of interest: the planar reflector (Chen *et al.* 1997; Ueda and Ozawa 1985) and the reference phantom (Wang and Shung 1997; Yao *et al.* 1990) methods. With both approaches, instrumentation effects are canceled out by dividing the PSD of the interrogated tissue by that of the reflector/phantom (see later Fig. 2). In the planar reflector technique, employed mainly in fundamental research using single-element transducers, the frequency response of the instrumentation is characterized by means of a smooth plate of known reflectivity (typically stainless steel, Plexiglas or quartz). The reflector surface creates a high-amplitude RF echo of short duration (*i.e.*, an impulse), which is gated out and used to estimate the spectral response of the instrumentation. The main advantage of this method is that it needs no prior information other than the geometry of the transducer and the reflectivity of the planar surface. In the reference phantom technique, commonly used with clinical array transducers, a well-characterized physical medium (*i.e.*, with known attenuation, speed of sound and BSC) is insonified with the same instrumentation parameters used to query the tissue. This method has special requirements for the acoustic properties of the reference medium; in particular, its speed of sound and attenuation must be close to those of the interrogated tissue (Ghoshal *et al.* 2013).

For most scattering tissues, the BSC presents an intrinsic stochastic behavior as it depends on the random position of scatterers (Insana and Brown 1993; Insana *et al.* 1990; Teisseire *et al.* 2010) or, for spatially correlated scatterers, on the pair-correlation function describing the relative position of their structures, which is also a random process (Fontaine *et al.* 1999; Franceschini and Cloutier 2013; Saha and Kolios 2011; Savéry and Cloutier 2001). Likewise, the measurement of BSC is affected by electronic noise, which is also stochastic by nature. Thus, to obtain a robust estimate of the BSC, coherent image compounding was implemented by averaging decorrelated spectra from multiple locations of the investigated tissue (Chen *et al.* 2005) or from the same location in multiple frames with different angles of observation (Gerig *et al.* 2004). Another approach consisted of deforming the tissue by applying an external pressure to obtain different signatures (Herd *et al.* 2011). Alternatively, several decorrelated temporal frames taken over the same region of interest (ROI) can be averaged to

obtain a good BSC estimate in the case of fast-moving tissues (*e.g.*, heart, vessel walls and flowing blood). However, with conventional focusing imaging, this usually requires gating and averaging over several cardiac cycles because of the limited frame rate.

The reduction of the stochastic nature of the BSC and the availability of a high frame rate to improve spectral tissue characterization can be addressed using ultrafast imaging (UI) techniques. Recent hardware improvements, such as graphic processing units, have enabled their use for real-time applications (Tanter and Fink 2014). Theoretically, UI techniques can offer thousands of frames per second (Montaldo *et al.* 2009). Moreover, these techniques can improve the image quality in terms of lateral resolution and contrast-to-noise ratio in the full field of view (Garcia *et al.* 2013). These latter studies indicated that the image quality is comparable to that of multi-focus techniques, but with an increase in effective frame rate.

One of the most common techniques for UI is plane wave imaging (PWI). In contrast to the traditional line-by-line formation of B-mode images using conventional focused beams, PWI uses all elements of an array transducer to emit a series of plane waves (Fig. 1a, b) and receive resulting echoes. Plane wave imaging results in diffraction hyperbolas (Fig. 1a), which must be collapsed in a process called migration, or beamforming (Fig. 1b), to generate an image. Several migration techniques have been proposed, including delay-and-sum reconstruction (Montaldo *et al.* 2009) and spectral domain signal interpolations (Garcia *et al.* 2013; Lu 1997). To produce a B-mode image, migrated frames steered at different angles are averaged to improve the lateral resolution with compounding (Fig. 1c).

Backscatter coefficient estimation using PWI has recently been validated *in vitro* for isotropic media (*i.e.*, a tissue producing similar echoes independent of the angle of insonification) (Garcia-Duitama *et al.* 2014; Salles *et al.* 2014). However, several biological tissues present anisotropic characteristics. In such cases, compounding of images from different angles could induce a biased BSC estimation as different information is averaged. We therefore expected, in this study, to evidence a bias in the characterization of anisotropic media, caused by the directivity of scatterers.

This study thus aimed to validate experimentally the possibility of using PWI to estimate BSCs in isotropic and anisotropic media. We specifically intended verifying the effect on BSC of single-angle insonifications (Fig. 1b) and compounded images (Fig. 1c). The validity of the results was confirmed by comparing BSCs with those obtained with single-element transducers and conventional focusing imaging (FI).

## METHODS

### Overview

To assess the accuracy of BSCs estimated with PWI data, two sets of experiments were conducted under both isotropic and anisotropic conditions. For the isotropic case, two tissue-mimicking phantoms with spherical scatterers were employed. For the anisotropic condition, porcine flowing blood in a tube circuit was used, as it can depict backscatter angular dependencies (Allard et al. 1996).

Experiments are portrayed in four sections. First, BSC estimates of both media were obtained from PWI compounded images (Fig. 1c) and PWI single-angle images (Fig. 1b). Second, BSC estimates of both media were compared with two benchmark BSCs obtained with single-element transducers and with conventional FI. Third, BSC estimates were fitted to appropriate scattering models to assess the effect of the beamforming technique on derived effective scatterer sizes. Finally, scatterer sizes from PWI single-angle acquisitions were used to assess the angular independency or dependency (*i.e.*, isotropy or anisotropy) of the scanned medium. Figure 2 summarizes the acquired data sets and their purpose for estimation of the BSC. Signal processing was performed using MATLAB (Version 2010a, The MathWorks, Natick, MA, USA).

### Description of phantoms

Two tissue-mimicking phantoms were bought from the University of Wisconsin at Madison. They were molded using an acrylic cylindrical ring 15 cm in diameter and 4 cm in height (Fig. 2). A 25- $\mu\text{m}$ -thick Saran wrap layer acted as an acoustic window on top and bottom planar surfaces. The tissue-mimicking material of both phantoms was made of agar at a mass fraction of 2%. Each phantom contained 4.5 g/L soda lime glass

spherical scatterers with a diameter of  $42.3 \pm 1.1 \mu\text{m}$  (Duke Fisher Catalog No. 09-980-090, Thermo Fisher Scientific, Waltham, MA, USA) or  $49.0 \pm 1.4 \mu\text{m}$  (Duke Fisher Catalog No. 09-980-091); these phantoms are labeled Duke40 and Duke50, respectively.

### Porcine blood experimental setup

Experimental conditions described by Yuan and Shung (1988a, 1988b) were replicated in this section. Briefly, three porcine blood samples of 2.5 L each were collected from a local slaughterhouse. After centrifugation, the buffy coat was removed, and the hematocrit was adjusted to 3% or 45% in autologous plasma. The blood was circulated in a steady flow system (Fig. 3). The circuit included a nearly horizontal (inclined by  $3^\circ$ ) polyvinyl chloride (PVC) tube (length = 130 cm, inner diameter = 2.5 cm) that ensured a fully developed laminar flow at measured speeds. An acoustic window made of agar at a mass fraction of 3% was placed 115 cm downstream from the tube entrance. The flow was controlled with a relief valve and measured with an electromagnetic flowmeter (Model FM-701 D, Carolina Medical Electronics, East Bend, NC, USA). Flow was adjusted to create mean shear rates of 2 and  $10 \text{ s}^{-1}$ , using the definition of Yuan and Shung (1988a). Blood was pumped from the lower to the upper reservoir using a peristaltic pump (Model 5000, Sarns, Ann Arbor, MI, USA), to avoid erythrocyte hemolysis.

### Array transducer acquisition protocol (for FI and PWI)

Both conventional focusing and plane wave data sets were acquired with SonixRP and SonixTouch systems (Ultrasonix Medical, Analogic, Boston, MA, USA) for phantoms and blood experiments, respectively. Both systems were equipped with a L14-5/38 linear array transducer (38-mm width, 128 elements, 9.5-MHz center frequency, 5- to 14-MHz  $-6\text{-dB}$  bandwidth).

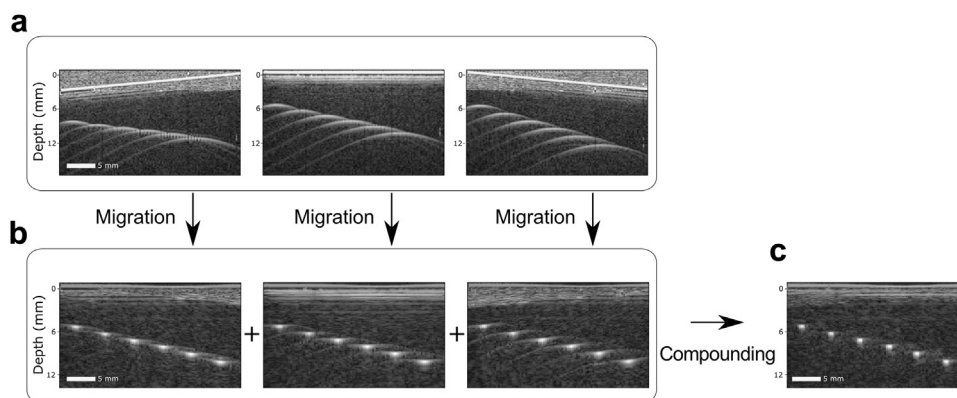


Fig. 1. Process for formation of plane wave images. (a) Envelope-detected radiofrequency images insonified at  $-10^\circ$ ,  $0^\circ$  and  $10^\circ$ . (b) Migrated images showing a lack of lateral resolution. Note that beamforming artifacts depend on the angle of insonification after migration. (c) Compounded image with restored lateral resolution.

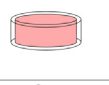
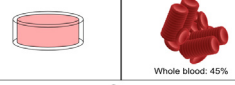
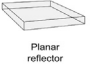
Required RF spectra	Transducer type	
	Single element	Linear array
Sample (phantom/tissue)		
	$S_{SS}$	$S_{SA}$
Reference for instrumentation compensation		
	$S_{PS}$	$S_{RA}$
BSC estimation	$BSC_{SS} \sim S_{SS}/S_{PS}$	$BSC_{SA} \sim S_{SA}/S_{RA} \cdot BSC_{PS}$

Fig. 2. Spectra required for instrumentation compensation during backscatter coefficient (BSC) estimation using different setups. The first letter of the spectrum subscripts indicates the interrogated medium (S = tested sample, P = planar reflector, R = reference medium); the second letter denotes the instrument used (S = single-element transducer, A = array transducer). Complete expressions for BSC estimation are given in eqns (2) and (4) for the reference medium and planar reflector techniques, respectively. For phantoms,  $BSC_{RS}$  was experimentally estimated using the planar reflector technique. For the erythrocyte suspension,  $BSC_{RS}$  was analytically calculated from a blood scattering model.

For phantoms, the transducer was translated in the elevation direction using ultrasound gel to acquire decorrelated signals. For blood, the transducer was placed in contact with the acoustic window over the axis of the PVC tube, as represented in Figure 3. The same system parameters (*i.e.*, pulse shape, voltage, gain) were used to insonify the tested sample and the reference medium (used in the reference phantom technique illustrated in Fig. 2).

The clinical software Exam Version 6.0.7 of the Ultrasonix scanners was used to acquire the conventional FI data set. The beam was focused at a 2.0-cm depth for phantom data and at a 3.0-cm depth for porcine blood

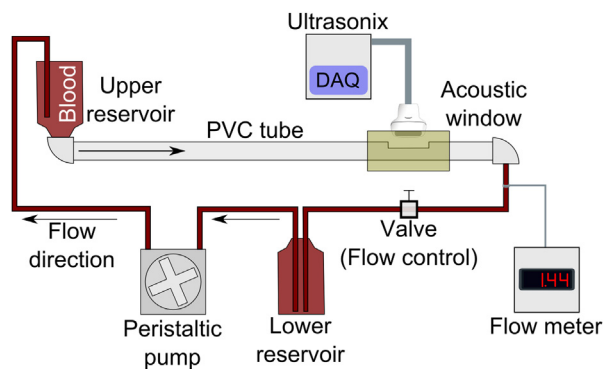


Fig. 3. Experimental setup used for estimating backscatter coefficients of porcine flowing blood. Blood is pumped from a lower to an upper reservoir, where height differences cause a non-pulsatile flow. Ultrasound images are acquired through an acoustic window in agar placed toward the end of the tube entrance. The entrance length allowed a laminar steady flow.

experiments. One hundred frames containing 128 scan lines each were acquired with an aperture varying from 16 to 32 elements, depending on the lateral position of active elements. All images were acquired at a depth of 7 cm with a frame rate of 33 Hz. The raw RF data were sampled at 40 MHz and recorded directly from the Exam software interface.

Plane waves were generated using the Ultrasonix beamforming library (Texo 6.0.7) for focused beams with a far focus at 30 cm. RF raw data were recorded on the SonixDAQ archiving system (Ultrasonix) and sampled at 40 MHz. For phantoms, the transmission protocol consisted of five steered plane wave insonifications at  $\pm 10^\circ$ ,  $\pm 5^\circ$  and  $0^\circ$ . For blood, angular insonifications were increased to  $\pm 15^\circ$ ,  $\pm 10^\circ$ ,  $\pm 5^\circ$  and  $0^\circ$  (see Fig. 4a) to evidence possible anisotropic effects. All images were acquired at a depth of 7 cm with a frame rate before compounding of 514 Hz (equivalent to 102 and 73 Hz after compounding for phantom and blood experiments, respectively).

The single-angle images were beamformed using the “delay-and-sum” technique described in detail by Montaldo *et al.* (2009) and using an  $f$ -number of 2. Compounded images were reconstructed as the average of a complete set of migrated steered insonifications, as illustrated in Figure 1c.

#### Speed of sound and attenuation coefficient

To compute BSCs with signal loss compensation, both two-way travel and signal attenuation are required.

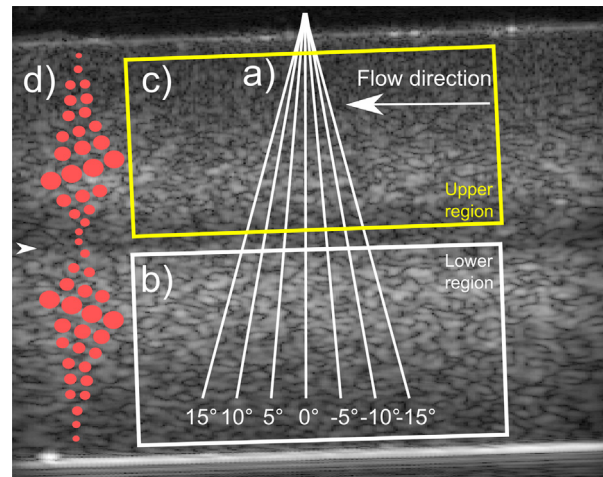


Fig. 4. Ultrasound B-mode image of porcine blood flowing into the circuit of Figure 3. The arrowhead to the left indicates the focal distance used for focusing imaging. (a) Angles considered for plane-wave imaging steering of the wavefront. (b, c) Lower and upper regions of interest for backscatter coefficient analysis. (d) Schematic representation of the orientation of flowing erythrocyte aggregates, inspired by Figure 9 of Qin *et al.* (1998) and used to interpret the effective scatterer radius analysis of Figure 10.

For phantoms, speed of sound and attenuation were measured experimentally using the substitution method detailed in Shung (2005). Two single-element transducers were employed to cover the bandwidth of the array transducer used for plane wave imaging. The first single-element transducer had a  $-6$ -dB bandwidth of 4.2–10.5 MHz (center frequency of 7.5 MHz) and an  $f$ -number of 4, whereas the second one had a  $-6$ -dB bandwidth of 10.9–32.3 MHz (center frequency of 20 MHz) with an  $f$ -number of 3. The attenuation coefficient  $\alpha_S$ , expressed in decibels per centimeter, was computed by fitting the experimental data to the power-law equation  $\alpha_S = \beta f^n$ , where  $\beta$  and  $n$  are coefficients to be estimated (Sehgal and Greenleaf 1982). This phenomenologic model was selected as it is regularly used on ultrasound attenuation data sets (Prince and Links 2006). For blood, the speed of sound was assumed at 1580 m/s for all hematocrits (Bushberg et al. 2002). Blood attenuation was considered to be 0.26f dB/cm at 45% hematocrit and 0.006f dB/cm at 3% hematocrit, where  $f$  is expressed in megahertz (Wang and Shung 1997).

#### Definition of regions of interest

The ROI was defined as the segment of the image that was used to estimate the BSC. As local artifacts could appear in images because of different beamforming strategies, some depths and lateral regions were consistently excluded. For conventional FI and single-element transducers, regions far from the focal zone were not used because of the low signal-to-noise ratio (SNR). For PWI, artifacts appearing in lateral regions because of beam steering and grating lobes were also excluded (see later the description of Fig. 9a, b). For phantoms, the selected ROIs were within the 12- to 35-mm image depth (*i.e.*,  $-6$ -dB focal zone), excluding 5 mm laterally on both sides of images (*white box* in Fig. 9a). For blood, the ROI was positioned to reproduce that used by Yuan and Shung (1988a). It consisted of the distal half of the tube ranging from 23 to 35 mm in depth, as represented by the white rectangle of Figure 4b.

#### Spectral estimation

To process the signal in the frequency domain, the Welch method for spectral smoothing was applied (Semmlow 2004; Welch 1967). Briefly, RF lines in the ROI were segmented with squared windows of  $15\lambda$  of side and 75% of overlap between them. RF lines inside each window were zero padded to 128 samples and multiplied by a Hann window before computing a power spectrum. It was assumed that all RF segments inside a window shared the same acoustic properties. The power spectra of every window inside the ROI were averaged to obtain a mean power spectrum

for each sample (*e.g.*, to obtain  $S_{SA}$  or  $S_{RA}$  in Figure 2, for the tested sample and the reference medium, respectively).

#### Signal processing for BSC estimation using an array transducer

For conventional focusing and plane wave data sets, the BSC was calculated using the reference phantom technique as

$$\text{BSC}_{SA}(f, d) = \frac{S_{SA}(f, d) 10^{\frac{\alpha_S(f, 2d)}{10}}}{\langle S_{RA}(f, d) 10^{\frac{\alpha_R(f, 2d)}{10}} \rangle_d} \text{BSC}_{RS}(f, d), \quad (2)$$

where  $S_{SA}$  and  $S_{RA}$  represent power spectra of the tested sample and the reference medium, respectively;  $\alpha_S$  and  $\alpha_R$  are attenuation coefficients of the latter media, respectively;  $\langle \cdot \rangle_d$  corresponds to the spectrum averaged from all windows found at depth  $d$ ; and  $\text{BSC}_{RS}$  is the known BSC from the reference medium. Note that in all cases,  $S_{RA}$  was acquired with the same beamforming strategy used for  $S_{SA}$ . In particular, for single-angle images in PWI,  $S_{RA}$  was calculated from temporal frames at the same angle of insonification used for the tested sample.

For phantoms,  $\text{BSC}_{RS}$  was obtained experimentally with single-element transducers and the planar reflector technique, as detailed later under Estimation of the BSC of Phantoms with a Single-Element Transducer. Both Duke40 and Duke50 phantoms were used as tested sample and reference as follows: during BSC estimation of the Duke40 phantom (*i.e.*, when it was considered as the sample phantom,  $\text{BSC}_{SA}$ ), the Duke50 single-element data set was used as the well-characterized reference,  $\text{BSC}_{RS}$ , and *vice versa*.

For porcine blood, the reference medium consisted of a suspension of erythrocytes in saline at a low hematocrit, as suggested by Wang and Shung (1997). We considered a suspension at 3% hematocrit flowing in the same circuit of Figure 2 at a mean shear rate of  $2 \text{ s}^{-1}$ . The saline medium restrains the formation of erythrocyte aggregates, thus providing a reproducible reference whatever the donor.  $\text{BSC}_{RS}$  was analytically calculated employing the state-of-the-art effective medium and structure factor model (EMTSFM) for blood scattering (Franceschini and Cloutier 2013; Franceschini et al. 2011), as

$$\text{BSC}_{RS-3\%}(f, s) = m(h_{\text{agg}}) \sigma(f, s, \gamma_z) S(h_{\text{agg}}, f, s), \quad (3)$$

where  $m$  is the number density of aggregates in the medium that depends on the volume fraction of aggregates,  $h_{\text{agg}}$  (calculated as the ratio of the hematocrit  $h$  to the volume fraction of erythrocytes into an aggregate, defined as the internal hematocrit  $h_i$ );  $\sigma(f, s, \gamma_z)$  is the backscatter

cross-section of an aggregate that depends on the insonifying frequency,  $f$ , the effective radius of the erythrocyte aggregate,  $s$ , and the acoustic impedance contrast between the suspending medium (saline in this case) and erythrocyte aggregates,  $\gamma_z$ ;  $S$  is the structure factor depending on  $h_{\text{agg}}$ , the frequency and the aggregate effective radius. To model the erythrocyte saline solution (*i.e.*, the reference medium with no aggregation), the aggregate in eqn (3) was considered to contain a single erythrocyte; thus, the following parameters were assumed:  $h = 3\%$ ;  $h_i = 100\%$ ;  $s = 2.7 \mu\text{m}$ ; and  $\gamma_z = 0.13$  (Franceschini and Cloutier 2013). The frequency range in eqn (3) matched the bandwidth of the array transducer. The structure factor  $S$  was approached by an analytical solution for solid spheres (Wertheim 1963), as proposed in the original description of the EMTSFM.

#### Comparison of estimated PWI BSCs with benchmark BSCs

To validate the accuracy of BSCs estimated with PWI, they were compared with two benchmarks: the BSC estimated with a single-element transducer and that obtained with FI. For phantoms, the single-element transducer BSC was experimentally measured by applying the planar reflector technique, as detailed in the next section. For porcine blood, the BSC measured with a single-element transducer was taken from the literature (Yuan and Shung 1988b). Quantitative error comparisons were done with the FI BSC data sets.

#### Estimation of the BSC of phantoms with a single-element transducer

The same single-element transducers used for speed of sound and attenuation coefficient estimation were used for this experiment. The definition of the ROI and the spectral estimation method were identical to those used for BSC estimation using the linear array transducer.

To obtain  $S_{\text{SS}}$  (Fig. 2), RF data were acquired scanning the phantoms with each transducer controlled by a 3-D positioner. Phantoms were submerged in degassed water at 22°C. Each transducer was positioned perpendicular to the phantom surface, and its focal point at 2-cm depth was located in the middle of the phantom. Then, the transducer was moved laterally to acquire nine spatially decorrelated images composed of at least 61 scan lines, each separated by a beam width. The beam width was estimated as  $1.02 \times \lambda \times f\text{-number}$  (Cobbold 2007), where  $\lambda$  is the wavelength in water at 22°C at the transducer central frequency.

To obtain  $S_{\text{PS}}$  (Fig. 2), RF data from the planar reflector were acquired at different depths of the focal zone. The transducer was first positioned at a distance corresponding to the proximal edge of the  $-6\text{-dB}$  region.

Then, it was moved axially away from the Plexiglas surface, with a step of half of a wavelength, until the Plexiglas surface coincided with the distal edge of the  $-6\text{-dB}$  focal region. At each step, a single scan line was acquired.

#### Signal processing for BSC estimation in phantoms using a single-element transducer

To obtain BSCs from phantoms with a single-element transducer, the planar reflector technique and the diffraction correction of Chen *et al.* (1997) were applied. The BSC of each window within a ROI was calculated as

$$\text{BSC}_{\text{SS}}(f, d) = \frac{S_{\text{SS}}(f, d) \cdot 10^{-\frac{\alpha_s(f, 2d)}{10}}}{S_{\text{PS}}(f, d)} \cdot r^2 \cdot D. \quad (4)$$

In eqn (4),  $S_{\text{SS}}$  and  $S_{\text{PS}}$  are power spectra of the tested phantom sample and of the planar reflector at frequency  $f$  and depth  $d$ , respectively;  $\alpha_s$  is the attenuation coefficient of the interrogated sample;  $r$  is the pressure reflection coefficient of the planar reflector, assumed as 0.37 for Plexiglas in degassed water (Han *et al.* 2013); and  $D$  is the beam diffraction correction function of Chen *et al.* (1997) given by

$$D(f, d) = 2.174 |E(f, d)|^2 \frac{d^2}{A_0 Z} \quad (5)$$

$$\text{with } E(f, d) = 1 - e^{-iG_p} [J_0(G_p) + iJ_1(G_p)]$$

In the latter equations,  $d$  is the depth of the window;  $A_0$  is the transducer active area;  $Z$  is the lateral size of the window used to gate out the RF signal;  $G_p$  is the pressure-gain factor, defined as  $G_p(f, d) = A_0 f / c_s d$ , where  $c_s$  is the speed of sound; and  $J_0$  and  $J_1$  are the zero- and first-order Bessel functions of the first kind, respectively.

#### Quantitative assessment of PWI BSCs

The mean deviation between BSCs computed with PWI and FI data sets was calculated, in decibels, as

$$\text{Dev}(\text{BSC}_{\text{PWI}}, \text{BSC}_{\text{FI}}) = \frac{1}{\|B\|} \sum_{f \in B} \left| 10 \log \left( \frac{\text{BSC}_{\text{PWI}}(f)}{\text{BSC}_{\text{FI}}(f)} \right) \right|, \quad (6)$$

where  $B$  is the set of frequencies in the analyzed bandwidth; and  $\text{BSC}_{\text{PWI}}(f)$  and  $\text{BSC}_{\text{FI}}(f)$  are mean BSCs calculated from a set of nine images (frames) with PWI and FI, respectively. For PWI, mean BSCs were determined from single-angle images and from steered images that were compounded in the time domain to compute a mean BSC. Deviations in eqn (6) were averaged for both phantoms and for both shear rates in the case of flowing blood.

### Derived BSC scatterer size and anisotropy assessment

To assess the effect of the beamforming technique on quantitative tissue characterization parameters, estimated BSCs were fitted to a scattering model appropriate to each medium. In this study, only the effective scatterer radius was estimated as the scatterer concentrations are known. For phantoms, the [Faran \(1951\)](#) model was chosen as it accurately describes randomly distributed rigid spheres in a homogeneous medium. This model considers physical and mechanical properties for both scatterers and the medium (*i.e.*, mass density, speed of sound and, for scatterers, Poisson ratio, radius and number density). For soda lime glass scatterers, these properties were considered to be a mass density of 2.38 g/cm<sup>3</sup>, Poisson ratio of 0.23, speed of sound of 5620 m/s ([Ide 1937](#)) and known-number densities of 0.05 and 0.03 million scatterers/mL for Duke40 and Duke50, respectively. Speed of sound and mass density of the background medium were measured as 1530 m/s and 1.01 g/cm<sup>3</sup>, respectively.

For blood, the EMTSFM scattering model of eqn (3) was selected as it takes into account coherent scattering caused by the high number density of red cell aggregates. We assumed spherical aggregates with an internal hematocrit  $h_i$  of 74% (*i.e.*, the maximum volume concentration of solid spheres in hexagonal close packing) ([Franceschini and Cloutier 2013](#)). The acoustic impedance contrast  $\gamma_z$  was again fixed at 0.13; the hematocrit was experimentally fixed at 45%, and the remaining parameter to determine was the effective aggregate radius,  $s$ .

The criterion to minimize when determining the effective scatterer size was the normalized root-mean-square error between the experimental BSC<sub>SA</sub> and that predicted by the scattering model:

$$\hat{s} = \arg \min_s \left\{ \sqrt{\frac{1}{\|B\|} \sum_{f \text{ in } B} \left( \frac{\text{BSC}_{\text{SA}}(f) - \text{BSC}_M(f, s)}{\text{BSC}_M(f, s)} \right)^2} \right\}. \quad (7)$$

In this expression,  $\hat{s}$  is the estimated effective scatterer radius; BSC<sub>SA</sub> and BSC<sub>M</sub> are backscatter coefficients obtained experimentally and by the scattering model evaluated at the radius  $s$ , respectively. An exhaustive search was employed to solve the minimization problem within the bandwidth of 5 to 14 MHz. The range of  $\hat{s}$  obtained from PWI single-angle images (between  $-15^\circ$  and  $15^\circ$ ) was used to assess the anisotropy.

## RESULTS

### Speed of sound and attenuation of phantoms

Speeds of sound were estimated as  $1533 \pm 3$  and  $1536 \pm 3$  m/s for Duke40 and Duke50, respectively. Attenuation coefficients for both phantoms were identical

at  $\beta = 0.034 \pm 0.01$  and  $n = 1.67 \pm 0.3$  in the bandwidth range of 5 to 14 MHz. These values also accounted for the transmission loss between the Saran wrap layer and the phantom itself. The numerical similarity of these acoustic measures for both phantoms ensures that beam diffraction was similar and that the reference phantom technique was suitable for instrumentation compensation. Because both phantoms had the same mean attenuation, estimated BSC<sub>SA</sub> using the reference phantom technique was dependent only on the BSC<sub>RS</sub> of the reference medium and on estimated power spectra  $S_{\text{SA}}$  and  $S_{\text{RA}}$  (eqn [2]).

### BSCs estimated using plane wave imaging versus benchmark measures

Mean BSCs for both isotropic phantoms are illustrated in [Figure 5](#). Standard deviations are hidden for clarity. The *solid and dashed lines* represent benchmark BSCs obtained with single-element transducers. The overlap of results suggests consistency in BSC estimation for all imaging techniques.

For blood experiments, samples from three swine were analyzed at two shear rates. The lower shear rate ( $2 \text{ s}^{-1}$ ) promoted the formation of larger erythrocyte aggregates, which increased the BSC magnitude. BSCs are presented comparing the two benchmarks (*i.e.*, single-element transducer and FI, [Fig. 6](#)) and all PWI techniques versus FI ([Fig. 7](#)). First, we observe agreement in magnitude and slope between BSCs obtained with FI and those from the literature at a normal fibrinogen concentration

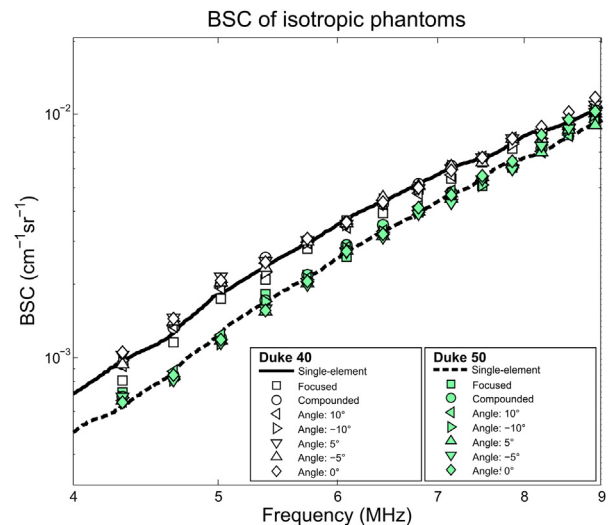


Fig. 5. Mean backscatter coefficient (BSC) from isotropic phantoms after averaging of nine image frames. *Solid and dotted lines* represent benchmark BSCs measured with single-element transducers. *Hollow and filled markers* represent BSCs estimated for focused, compounded and single-angle plane wave images for Duke40 and Duke50 phantoms, respectively. Focused and all plane wave techniques reproduced consistently benchmark BSCs. Standard deviations are hidden for clarity.

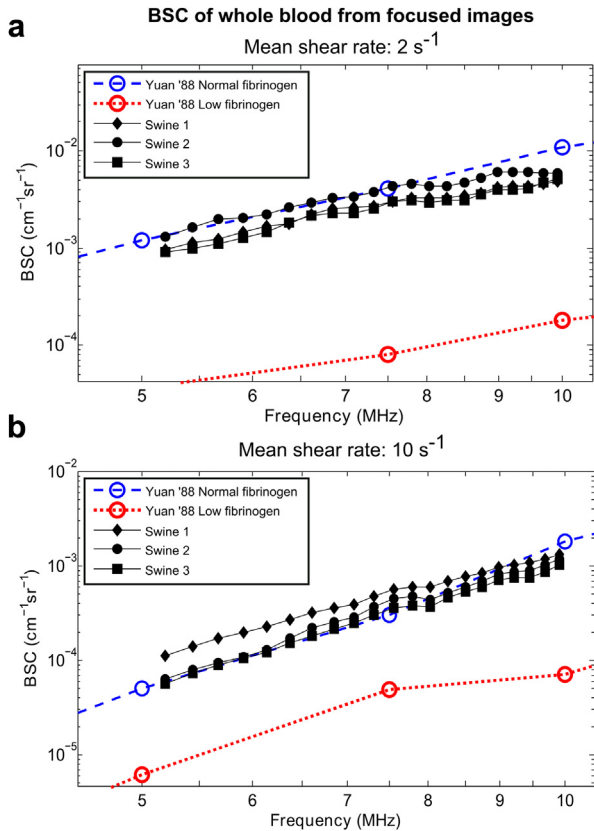


Fig. 6. Mean backscatter coefficients (BSCs) of porcine flowing blood estimated with conventional focusing imaging at mean shear rates of  $2 \text{ s}^{-1}$  (a) and  $10 \text{ s}^{-1}$  (b). Dotted blue and red lines are BSC estimations made with a single-element transducer at normal and low plasma fibrinogen concentrations, respectively (data taken from Yuan and Shung 1988b). Less erythrocyte aggregation and smaller BSCs are obtained at a low fibrinogen level (Weng *et al.* 1996a, 1996b). Filled markers represent the BSCs estimated from blood samples of three swine.

(Fig. 6). This agreement validates the use of the EMTSFM to produce the reference BSC<sub>RS</sub> and also confirms that attenuation and beam diffraction were correctly compensated for during the estimation process. From Figure 6, it is also observed that inter-individual differences were present for the three swine. BSCs from compounded data matched well those of FI in magnitude and spectral slope in most cases (with the exception of swine 1 at  $2 \text{ s}^{-1}$ ) (Fig. 7). However, the anisotropy of blood backscatter affected, as expected, the BSC magnitude at each single angle. A consistent incremental bias in BSC was observed for step changes in insonifying angles (see the description of Fig. 10 for a better visualization of the anisotropy).

#### Quantitative comparisons of PWI BSCs to benchmark FI BSCs

Mean deviations (eqn [6]) of PWI beamforming techniques are illustrated in Figure 8. For phantoms,

deviations below 0.26 dB on average were observed. For blood experiments, mean deviations ranged from 1.1 to 2.2 dB. The lowest deviation was obtained with the compounded approach.

#### BSC artifacts induced by the beamforming protocol

Tissue-mimicking phantoms were considered to have a reasonably homogeneous scatterer distribution. Therefore, the entire analyzed volume should share similar BSCs. We used this fact to identify image regions with systematic artifacts produced by selected beamforming techniques. Figure 9 depicts parametric images of the mean deviation (eqn [6]) computed for selected PWI versus FI methods in the case of Duke50 phantom. Overall, errors were not dependent on depth, suggesting that the attenuation was correctly compensated for and that the SNR was sufficient to allow good BSC estimations. Plane wave-steered images (Fig. 9a, b) revealed, as expected, lateral artifacts because of the reduced coherent acoustic energy in these regions. Remarkably, the  $0^\circ$  data set also presented lateral artifacts (Fig. 9c). These artifacts were also present in the compounded image, although attenuated (Fig. 9d). As mentioned earlier, those lateral regions were excluded from all data analyses.

#### Derived scatterer sizes and anisotropy assessment

The effective scatterer radii derived from the model fitting of phantom and blood experiments are shown in Table 1. In both cases, estimates from compounded PWI were in agreement with those of FI, with deviations of less than  $2.9 \mu\text{m}$ . For blood, PWI (compounded and single angles) and FI data sets revealed a maximum error of  $7.5 \mu\text{m}$  compared with single-element transducer measures from the literature (by fitting the EMTSFM model to the data of Yuan and Shung [1988b]). It is notable that radii of phantom scatterers were consistent for all single-angle measures. This may be attributed to the isotropy of embedded glass particles. In contrast, radii observed for steered images in blood appeared angle dependent.

This latter observation is better visualized in Figure 10. Left panels in this figure correspond to radii taken from the lower ROI of the blood vessel depicted by the white rectangle of Figure 4b, whereas results in right panels represent measures taken in the top yellow ROI of Figure 4c. As observed, the anisotropic behavior of scatterer radii was consistent from pig to pig. Increasing or decreasing trends were observed from measures taken at  $-15^\circ$  to  $15^\circ$ , depending on the position of the ROI within the tube.

## DISCUSSION

In this study, we estimated the BSC of two isotropic tissue-mimicking phantoms and anisotropic aggregating

## BSC of whole blood from plane wave and focused images

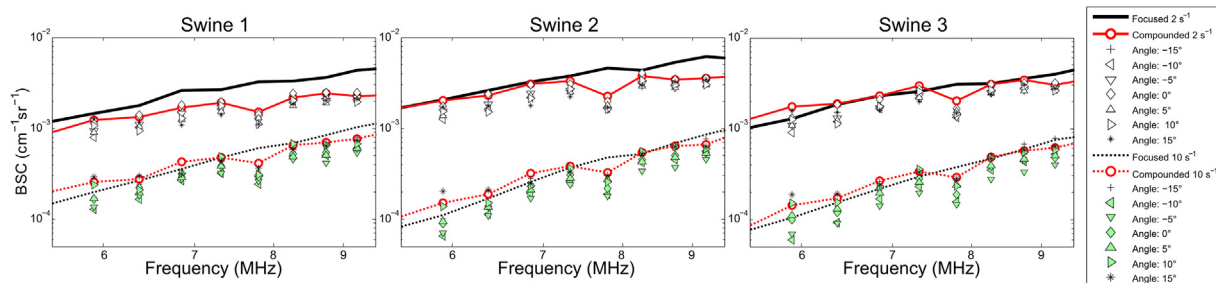


Fig. 7. Mean backscatter coefficients (BSCs) of porcine flowing blood estimated with compounded and single-angle plane wave images at mean shear rates of 2 and  $10 \text{ s}^{-1}$  compared with focused images.

erythrocyte structures using two PWI strategies: compounded and single-angle insonifications. In isotropic media, both PWI approaches provided accurate BSC estimations compared with benchmark measures. For flowing blood, even if mean deviations from benchmark BSC values were higher than with the phantom data sets (1.1–2.2 dB vs. 0.15–0.26 dB), it can be concluded that PWI gave satisfying estimations of the backscatter coefficient. Indeed, observed mean differences below 2.2 dB between PWI and FI BSCs are smaller than the inter-subject variability for porcine blood (approximately 3 dB) (Shung et al. 1992) and well below changes in BSC attributed to the kinetics of red blood cell aggregation (approximately 12 dB) (Yuan and Shung 1988b).

For blood experiments, single-angle PWI revealed angular dependencies of the effective scatterer size, which may be attributed to the macroscopic orientation of aggregates with flow streamlines, as postulated by Allard et al. (1996) and Qin et al. (1998). If one considers spherical aggregates, as assumed by the EMTSFM model, one should expect small aggregates near the vessel wall where the shear rate is maximum, larger aggregates near the tube center and smaller aggregates at the tube center axis because of the well-known “black hole” phenomenon (*i.e.*, the reduction of the aggregation when the shear rate is close to zero, see Yuan and Shung [1989] and Qin et al. [1998]). This is illustrated in Figure 4d.

With this latter figure, let us explain the results in Figure 10. In the lower region of the tube (*white rectangle*), scatterer sizes increased from  $-15^\circ$  to  $15^\circ$  insonification, likely because the macroscopic structure of aggregates was more perpendicular to the plane wave front at  $15^\circ$ . By opposite analogy, this also applies to the upper region (*yellow rectangle*) where larger scatterer sizes (higher backscatter) were observed at  $-15^\circ$ . Thus, this suggests that edges of flowing aggregates were tilted with a 3-D cone-shaped orientation into the cylindrical tube. An optical validation of this hypothesis has yet to be proven, but current technologies make this difficult

because of the opacity of blood at a normal hematocrit. However, this is consistent with previous observations of higher backscatter when perpendicular muscle fiber orientations are insonified (Recchia et al. 1995).

Even if results with compounded images were comparable to those of FI, the benefits of using plane waves to calculate the BSC are threefold. First, higher frame rates allow robust spectral characterization of fast-moving tissues such as the cardiac muscle, artery wall and pulsatile blood flow. This advantage may be used to characterize the BSC of transient events (*e.g.*, turbulent motion downstream of a stenosis) (Cloutier et al. 1995). This may also be advantageous to reduce the acquisition length while maintaining sufficient records of RF data to reduce the variance of BSC estimates with averaging. Second, the quality of images, evaluated by the lateral resolution and the contrast-to-noise ratio, had been shown by others to be comparable to that of multi-focus imaging in the whole field of view (Garcia et al. 2013; Montaldo et al. 2009). This property may favor the use of the whole image depth for BSC estimation in the opposite of conventional focusing imaging, where BSC estimation is expected to be better at the focus. Third, we found

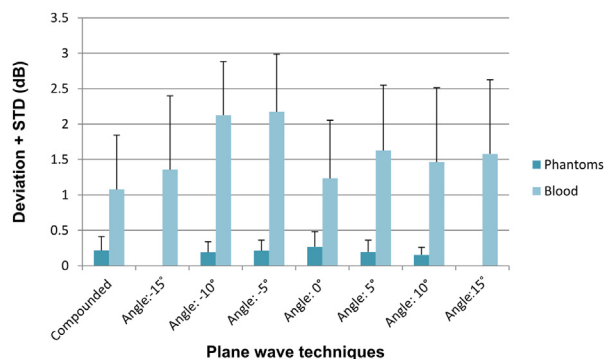


Fig. 8. Deviation of the backscatter coefficient (BSC) in decibels derived from plane wave techniques compared with the BSC of conventional focusing imaging. Data from phantoms are in dark blue, and those of porcine blood are in light blue. STD = standard deviation.

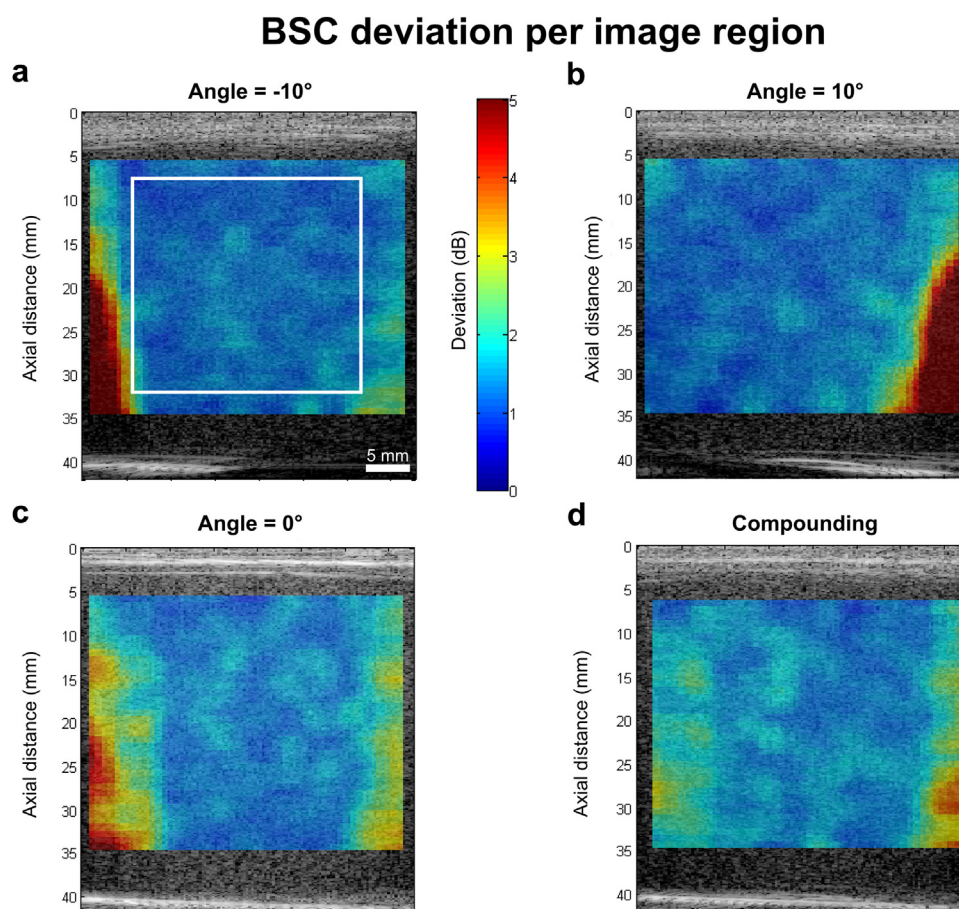


Fig. 9. Parametric images of the mean deviation of the backscatter coefficient (in dB) reveal regions with systematic artifacts induced by the beamforming protocol. Higher values (*red*) indicate regions with larger deviations from the benchmark backscatter coefficient (focused images). (a–c) Single-angle plane wave insonification at  $-10^\circ$ ,  $10^\circ$  and  $0^\circ$ , respectively; lateral biases caused by the steering of the wave front are observed. (d) Image compounded from plane wave insonifications; attenuated lateral biases are still present on both sides. The *white box* in (a) indicates the region of interest considered for backscatter coefficient analysis.

that the anisotropy of tissues can be assessed using the angular data available before compounding. This information is of medical relevance to study the myocardium (Mottley and Miller 1988), tendons (Hoffmeister *et al.* 1995) and aggregates of erythrocytes (Allard *et al.* 1996; Savéry and Cloutier 2005), to name a few examples.

Plane wave imaging-derived techniques, however, have limitations that may affect BSC estimation. First, beam penetration without compounding is more limited than with FI because the acoustic pressure of a plane wave insonification is lower, particularly at the focus. Conversely in PWI, if the frame rate is not of particular interest for a specific application, the use of several insonification angles could lead to a slightly better SNR for compounded images, thus leading to improved penetration. Nonetheless, the number of steered angles has a limit when one is concerned by SNR improvement

(Garcia *et al.* 2013). Other techniques coming from radar theory, like coded excitation and pulse compression (Oelze 2007), can lessen this drawback. Spectral analysis techniques have already been successfully used in conjunction with coded excitation (Kanzler and Oelze 2008; Sanchez *et al.* 2009).

A second drawback is the reduced lateral resolution affecting single-angle PWI images because of the lack of transmit focusing. However, the compounding process achieves a synthetic focusing for each pixel in the intersection of the beams, thus restoring the resolution (Montaldo *et al.* 2009). Nonetheless, similar problems could be present in compounded images if the beams of pre-compounded images do not overlap. The triangular region created by intersecting beams (Fig. 11) has been previously discussed in the context of elastography using multiple steered beams (Hansen *et al.* 2010). The depth at which beams cease to overlap and, as a consequence, at

Table 1. Effective radius of scatterers (in  $\mu\text{m}$ ) in phantoms (*i.e.*, glass beads) and blood (*i.e.*, erythrocyte aggregates) after fitting of their backscatter coefficients to appropriate scattering models\*

Sample	Mean shear rate	Single element	Focused	Compounded plane waves	Single-angle plane waves						
					$-15^\circ$	$-10^\circ$	$-5^\circ$	$0^\circ$	$5^\circ$	$10^\circ$	$15^\circ$
Duke40	NA	20.4	20.1	20.2	NA	20.3	20.3	20.2	20.4	20.1	NA
Duke50	NA	23.9	23.4	23.1	NA	23.2	23.3	23.3	23.7	23.5	NA
Swine 1	$2 \text{ s}^{-1}$	41.4 <sup>†</sup>	43.4	41.4	38.5	38.3	39.2	40.9	39.0	39.6	40.6
Swine 2			47.4	48.9	43.2	42.4	44.0	46.2	44.5	44.2	45.5
Swine 3			42.5	45.4	40.4	38.7	39.8	42.3	41.2	42.0	43.6
Swine 1	$10 \text{ s}^{-1}$	24.0 <sup>†</sup>	25.9	26.7	24.6	22.8	23.0	24.3	24.4	25.9	26.9
Swine 2			23.4	23.8	22.8	20.5	19.8	21.5	21.4	22.8	24.1
Swine 3			22.4	22.8	22.5	19.8	18.9	21.0	21.2	22.6	23.6

NA = not applicable.

\* For blood, backscatter coefficients from the lower region of interest of Figure 4 (white box) were considered. The actual radii of spheres within Duke40 and Duke50 phantoms were 21.1 and 24.5  $\mu\text{m}$ , respectively. The anisotropy of blood backscatter is evidenced when estimates from single angles are compared between them.

<sup>†</sup> Data from the literature. Inter-individual differences in aggregation of erythrocytes may exist with studied porcine blood samples.

which the lateral resolution is diminished is determined by the width of the transducer,  $m$ , and the maximal steering angle,  $\theta$  (see Fig. 11). This depth is described by the equation

$$d = \frac{m}{2 \tan(\theta)}. \quad (8)$$

In the present study, the lack of lateral resolution on single-angle images had no impact, as phantom and blood flow echogenicity was homogeneous in the horizontal direction with no hyper-echoic regions.

A third drawback is caused by beam steering, which affects not only PWI but other beamforming techniques employing oriented beams. As illustrated in Figure 9 (a, b), beam steering causes regions below the lateral side

of the transducer to receive less acoustic pressure than those below its center, potentially affecting the SNR of the BSC. In this study, the latter drawback was avoided by excluding lateral zones of each image as the depth scanned was far from the interception limit (corresponding to 10.8 cm for our transducer measuring  $m = 38 \text{ mm}$ ). However, for small probes (*e.g.*, arrays of 10 mm in lateral length), the resolution triangle can imply serious biases for BSC estimation, even at a depth as small as 3 cm. A possible approach to counteract this problem may consist of normalizing the sample power spectrum  $S_{SA}$  in eqn (2) with a set of windows in the reference medium having the same loss in acoustic energy (*i.e.*, the same position in the ROI). Nevertheless, to have a consistent estimate with the reference medium, it would be

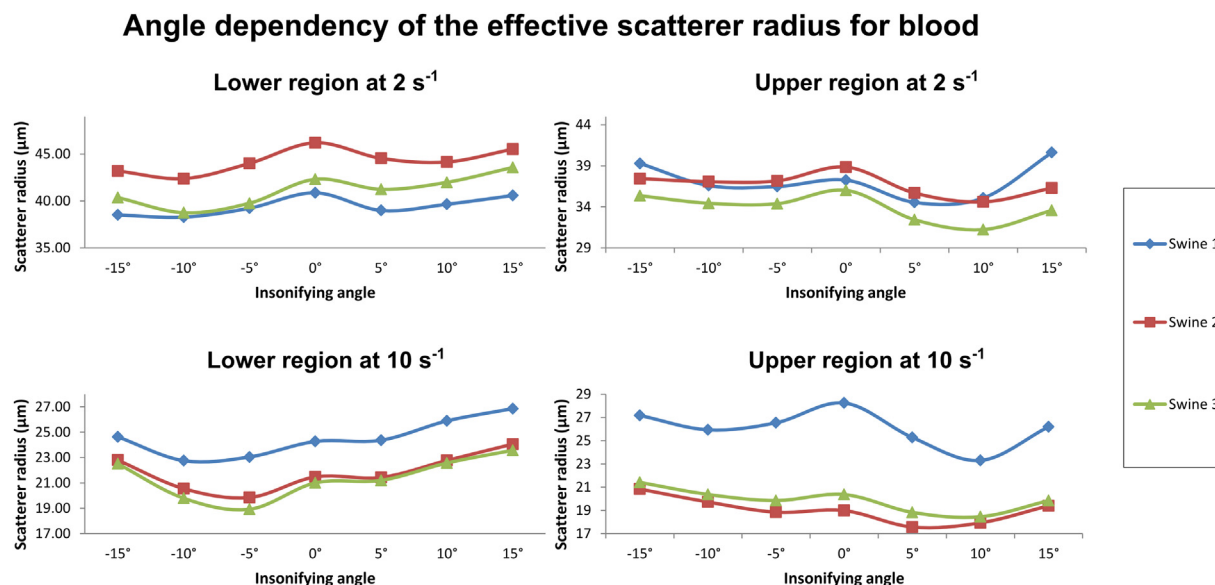


Fig. 10. Effective scatterer radius estimated from the fitting of the backscatter coefficient to a model of blood backscatter at shear rates of 2 and  $10 \text{ s}^{-1}$ . Raising and decreasing trends in scatterer dimensions are observed when considering lower and upper regions of interest depicted in Figure 4.

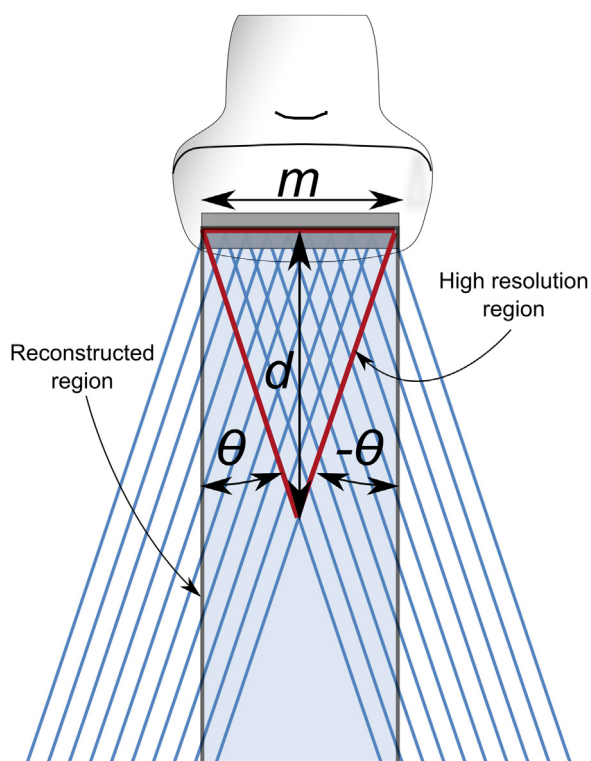


Fig. 11. Depiction of the triangle with a higher lateral resolution for plane-wave compounded images, defined by the intersection of single-angle plane-wave images. After a distance  $d$ , the gain in lateral resolution offered by compounding is lost and the backscatter coefficient estimation quality may be affected.

necessary to perform sufficient averaging of power spectra. With a static reference phantom, this may be difficult, but it may be possible in the case of flowing blood, as different time frames may be used.

One important aspect of our results is that they were obtained with a clinical scanner providing RF data and, in the case of FI, with the same software employed for patient examination. This provides more evidence of the possibility of integrating spectral tissue characterization methods into clinical practice, even with new beamforming technologies. Historically, the implementation of spectral-based quantitative ultrasound techniques on clinical scanners has been deferred for a few reasons; in particular, the lack of access to RF signals and the absence of a consensus on the methodology of BSC estimation were early problems (Anderson *et al.* 2010; Madsen *et al.* 1999; Nam *et al.* 2011). Today, most of these causes have been overcome. For example, several commercial ultrasound scanners provide easy access to RF data (before or after beamforming), thus facilitating the implementation of robust BSC spectral methods. State-of-the-art BSC estimation procedures can be found in recent textbooks (Franceschini and Cloutier 2013;

Ghoshal *et al.* 2013). Another issue delaying acceptance of quantitative spectral methods is the need for calibration of the backscatter signal intensity (Wear *et al.* 2005). It is common for most laboratories to create their own reference medium, making it difficult to reproduce measurements (*e.g.*, Salles *et al.* 2014; Wang and Shung 1997; Wear *et al.* 2005). Calibrated commercial tissue-mimicking phantoms would alleviate this problem (Nam *et al.* 2012). Other challenges, such as real-time display of parametric images, are still to be overcome; nevertheless, hardware improvements, such as graphic processing units, in addition to experimental validation as discussed here, allow us to be hopeful of a future clinical scanner with spectral characterization capabilities.

## CONCLUSIONS

Evidence suggesting the use of plane-wave imaging for the estimation of the backscatter coefficient in biological tissues was discussed. BSC estimates obtained with compounded plane-wave images were equivalent to those obtained with single-element transducers and conventional focusing, in both isotropic and anisotropic media. In particular, small differences were observed between effective scatterer radii derived from the two techniques. Additionally, we evidenced in experiments with porcine blood that single-angle PWI images (*i.e.*, before compounding) could be used to assess the anisotropy of flowing erythrocyte aggregates. These results suggest that plane-wave imaging can be used for spectral tissue characterization, particularly in the case of fast-moving tissues.

*Acknowledgments*—The authors acknowledge François Destrempe and Jeremy Kemmerer for valuable discussions, and Romain de Monchy for his assistance in blood experiments.—This work was financially supported by Canadian Institutes of Health Research Grant MOP-84358. Mr. Garcia-Duitama was recipient of a Ph.D. scholarship from the Natural Sciences and Engineering Research Council of Canada (Meditis Program of the Institute of Biomedical Engineering of the École Polytechnique and University of Montreal). He also received the Hydro-Québec scholarship award at the University of Montreal.

## REFERENCES

- Allard L, Cloutier G, Durand LG. Effect of the insonification angle on the Doppler backscattered power under red blood cell aggregation conditions. *IEEE Trans Ultrason Ferroelectr Freq Control* 1996; 43:211–219.
- Anderson JJ, Herd MT, King MR, Haak A, Hafez ZT, Song J, Oelze ML, Madsen EL, Zagzebski JA, O'Brien WD. Interlaboratory comparison of backscatter coefficient estimates for tissue-mimicking phantoms. *Ultrason Imaging* 2010;32:48–64.
- Bushberg JT, Leidholdt EM, Seibert AJ, Boone JM. *Ultrasound imaging*. In: John JR, Snyder A, DeGeorge T, (eds). *The essential physics of medical imaging*. Philadelphia: Lippincott Williams & Wilkins; 2002. p. 469–554.
- Chen Q, Gerig AL, Techavipoo U, Zagzebski JA, Varghese T. Correlation of RF signals during angular compounding. *IEEE Trans Ultrason Ferroelectr Freq Control* 2005;52:961–970.

- Chen X, Phillips D, Schwarz KQ, Mottley JG, Parker KJ. The measurement of backscatter coefficient from a broadband pulse-echo system: A new formulation. *IEEE Trans Ultrason Ferroelectr Freq Control* 1997;44:515–525.
- Cloutier G, Allard L, Durand LG. Changes in ultrasonic Doppler backscattered power downstream of concentric and eccentric stenoses under pulsatile flow. *Ultrasound Med Biol* 1995;21:59–70.
- Cobbold RS. *Foundations of biomedical ultrasound*. New York: Oxford University Press; 2007. p. 135–226.
- Faran JJ Jr. Sound scattering by solid cylinders and spheres. *J Acoust Soc Am* 1951;23:405–418.
- Fontaine I, Bertrand M, Cloutier G. A system-based approach to modeling the ultrasound signal backscattered by red blood cells. *Biophys J* 1999;77:2387–2399.
- Franceschini E, Metzger B, Cloutier G. Forward problem study of an effective medium model for ultrasound blood characterization. *IEEE Trans Ultrason Ferroelectr Freq Control* 2011;58:2668–2679.
- Franceschini E, Cloutier G. Modeling of ultrasound backscattering by aggregating red blood cells. In: Mamou J, Oelze ML, (eds). *Quantitative ultrasound in soft tissues*. Berlin/Heidelberg: Springer; 2013. p. 117–145.
- Garcia D, Tarnec L, Muth S, Montagnon E, Cloutier G. Stolt's  $f$ - $k$  migration for plane wave ultrasound imaging. *IEEE Trans Ultrason Ferroelectr Freq Control* 2013;60:1853–1867.
- Garcia-Duitama J, Han A, Chayer B, Garcia D, Oelze ML, Cloutier G. Experimental validation of plane wave imaging using  $k$ -space beamforming for spectral characterization of isotropic media. *Proc IEEE Ultrason Symp* 2014;2414–2417.
- Gerig AL, Varghese T, Zagzebski JA. Improved parametric imaging of scatterer size estimates using angular compounding. *IEEE Trans Ultrason Ferroelectr Freq Control* 2004;51:708–715.
- Ghoshal G, Mamou J, Oelze ML. State of the art methods for estimating backscatter coefficients. In: Mamou J, Oelze ML, (eds). *Quantitative ultrasound in soft tissues*. Berlin/Heidelberg: Springer; 2013. p. 3–19.
- Han A, Abuhabsah R, Miller RJ, Sarwate S, O'Brien WD Jr. The measurement of ultrasound backscattering from cell pellet biophantoms and tumors *ex vivo*. *J Acoust Soc Am* 2013;134:686–693.
- Hansen HHG, Lopata RGP, Idzenga T, De Korte CL. Full 2-D displacement vector and strain tensor estimation for superficial tissue using beam-steered ultrasound imaging. *Phys Med Biol* 2010;55:3201–3218.
- Herd MT, Hall TJ, Jiang J, Zagzebski JA. Improving the statistics of quantitative ultrasound techniques with deformation compounding: An experimental study. *Ultrasound Med Biol* 2011;37:2066–2074.
- Hoffmeister BK, Wong AK, Verdonk ED, Wickline SA, Miller JG. Comparison of the anisotropy of apparent integrated ultrasonic backscatter from fixed human tendon and fixed human myocardium. *J Acoust Soc Am* 1995;97:1307–1313.
- Ide JM. The velocity of sound in rocks and glasses as a function of temperature. *J Geol* 1937;689–716.
- Insana MF, Wagner RF, Brown DG, Hall TJ. Describing small scale structure in random media using pulse echo ultrasound. *J Acoust Soc Am* 1990;87:179–192.
- Insana MF, Brown DG. Acoustic scattering theory applied to soft biological tissues. In: Shung KK, Thieme GA, (eds). *Ultrasonic scattering in biological tissues*. Boca Raton, FL: CRC Press; 1993. p. 75–124.
- Kanzler SG, Oelze ML. Improved scatterer size estimation using backscatter coefficient measurements with coded excitation and pulse compression. *J Acoust Soc Am* 2008;123:4599–4607.
- Lizzi FL, Greenebaum M, Feleppa EJ, Elbaum M, Coleman DJ. Theoretical framework for spectrum analysis in ultrasonic tissue characterization. *J Acoust Soc Am* 1983;73:1366–1373.
- Lizzi FL, King DL, Rorke MC, Hui J, Ostromogilsky M, Yaremko MM, Feleppa EJ, Wai P. Comparison of theoretical scattering results and ultrasonic data from clinical liver examinations. *Ultrasound Med Biol* 1988;14:377–385.
- Lu JY. 2-D and 3-D high frame rate imaging with limited diffraction beams. *IEEE Trans Ultrason Ferroelectr Freq Control* 1997;44:839–856.
- Madsen EL, Dong F, Frank GR, Garra BS, Wear KA, Wilson T, Zagzebski JA, Miller HL, Shung KK, Wang S. Interlaboratory comparison of ultrasonic backscatter, attenuation, and speed measurements. *J Ultrasound Med* 1999;18:615–631.
- Montaldo G, Tanter M, Bercoff J, Benech N, Fink M. Coherent plane-wave compounding for very high frame rate ultrasonography and transient elastography. *IEEE Trans Ultrason Ferroelectr Freq Control* 2009;56:489–506.
- Mottley JG, Miller J. Anisotropy of the ultrasonic backscatter of myocardial tissue: I. Theory and measurements *in vitro*. *J Acoust Soc Am* 1988;83:755–761.
- Nair A, Kuban BD, Tuzcu EM, Schoenhagen P, Nissen SE, Vince DG. Coronary plaque classification with intravascular ultrasound radio-frequency data analysis. *Circulation* 2002;106:2200–2206.
- Nam K, Rosado-Mendez IM, Wirtzfeld LA, Kumar V, Madsen EL, Ghoshal G, Pawlicki AD, Oelze ML, Lavarello R, Bigelow T, Zagzebski JA, O'Brien WD Jr, Hall TJ. Cross-imaging system comparison of backscatter coefficient estimates from a tissue-mimicking material. *J Acoust Soc Am* 2012;132:1319–1324.
- Nam K, Rosado-Mendez IM, Wirtzfeld LA, Pawlicki AD, Kumar V, Madsen EL, Ghoshal G, Lavarello RJ, Oelze ML, Bigelow TA. Ultrasonic attenuation and backscatter coefficient estimates of rodent-tumor-mimicking structures: Comparison of results among clinical scanners. *Ultrasound Imaging* 2011;33:233–250.
- Oelze ML. Bandwidth and resolution enhancement through pulse compression. *IEEE Trans Ultrason Ferroelectr Freq Control* 2007;54:768–781.
- Oelze ML. Statistics of scatterer property estimates. In: Mamou J, Oelze ML, (eds). *Quantitative ultrasound in soft tissues*. Berlin/Heidelberg: Springer; 2013. p. 43–69.
- Prince JL, Links JM. *The physics of ultrasound*. In: *Medical imaging signals and systems*. Upper Saddle River, NJ: Pearson Prentice Hall; 2006.
- Qin Z, Durand LG, Cloutier G. Kinetics of the “black hole” phenomenon in ultrasound backscattering measurements with red blood cell aggregation. *Ultrasound Med Biol* 1998;24:245–256.
- Recchia D, Hall CS, Shepard RK, Miller JG, Wickline SA. Mechanism of the view-dependence of ultrasonic backscatter from normal myocardium. *IEEE Trans Ultrason Ferroelectr Freq Control* 1995;42:91–98.
- Sadeghi-Naini A, Papanicolau N, Falou O, Zubovits J, Dent R, Verma S, Trudeau M, Boileau JF, Spayne J, Iradji S, Sofroni E, Lee J, Lemon-Wong S, Yaffe M, Kolios CM, Czarnota JG. Quantitative ultrasound evaluation of tumor cell death response in locally advanced breast cancer patients receiving chemotherapy. *Clin Cancer Res* 2013;19:2163–2174.
- Saha RK, Kolios MC. Effects of cell spatial organization and size distribution on ultrasound backscattering. *IEEE Trans Ultrason Ferroelectr Freq Control* 2011;58:2118–2131.
- Salles S, Liebgott H, Basset O, Cachard C, Vray D, Lavarello R. Experimental evaluation of spectral-based quantitative ultrasound imaging using plane wave compounding. *IEEE Trans Ultrason Ferroelectr Freq Control* 2014;61:1824–1834.
- Sanchez JR, Pocci D, Oelze ML. A novel coded excitation scheme to improve spatial and contrast resolution of quantitative ultrasound imaging. *IEEE Trans Ultrason Ferroelectr Freq Control* 2009;56:2111–2123.
- Savéry D, Cloutier G. A point process approach to assess the frequency dependence of ultrasound backscattering by aggregating red blood cells. *J Acoust Soc Am* 2001;110:3252.
- Savéry D, Cloutier G. Effect of red cell clustering and anisotropy on ultrasound blood backscatter: A Monte Carlo study. *IEEE Trans Ultrason Ferroelectr Freq Control* 2005;52:94–103.
- Sehgal CM, Greenleaf JF. Ultrasonic absorption and dispersion in biological media: A postulated model. *J Acoust Soc Am* 1982;72:1711–1718.
- Semmlow J. *Biosignal and biomedical image processing: MATLAB based application*. New York: Marcel Dekker; 2004.
- Shung KK, Cloutier G, Lim CC. The effects of hematocrit, shear rate, and turbulence on ultrasonic Doppler spectrum from blood. *IEEE Trans Ultrason Ferroelectr Freq Control* 1992;39:462–469.

- Shung KK. Methods for measuring speed, attenuation, absorption, and scattering. In: *Diagnostic ultrasound: Imaging and blood flow measurements*. Boca Raton, FL: CRC Press; 2005. p. 185–202.
- Szabo TL. *Diagnostic ultrasound imaging: Inside out*. San Diego: Academic Press; 2004.
- Tanter M, Fink M. Ultrafast imaging in biomedical ultrasound. *IEEE Trans Ultrason Ferroelectr Freq Control* 2014;61:102–119.
- Teisseire M, Han A, Abuhabsah R, Blue JP Jr, Sarwate S, O'Brien WD Jr. Ultrasonic backscatter coefficient quantitative estimates from Chinese hamster ovary cell pellet biophantoms. *J Acoust Soc Am* 2010;128:3175–3180.
- Tripette J, Denault AY, Allard L, Chayer B, Perrault LP, Cloutier G. Ultrasound monitoring of RBC aggregation as a real-time marker of the inflammatory response in a cardiopulmonary bypass swine model. *Crit Care Med* 2013;41:e171–e178.
- Ueda M, Ozawa Y. Spectral analysis of echoes for backscattering coefficient measurement. *J Acoust Soc Am* 1985;77:38–47.
- Waag R, Nilsson J, Astheimer J. Characterization of volume scattering power spectra in isotropic media from power spectra of scattering by planes. *J Acoust Soc Am* 1983;74:1555–1571.
- Wang SH, Shung KK. An approach for measuring ultrasonic backscattering from biological tissues with focused transducers. *IEEE Trans Biomed Eng* 1997;44:549–554.
- Wear KA, Stiles TA, Frank GR, Madsen EL, Cheng F, Feleppa EJ, Hall CS, Kim BS, Lee P, O'Brien WD Jr. Interlaboratory comparison of ultrasonic backscatter coefficient measurements from 2 to 9 MHz. *J Ultrasound Med* 2005;24:1235–1250.
- Welch PD. The use of fast Fourier transform for the estimation of power spectra: A method based on time averaging over short, modified periodograms. *IEEE Trans Audio Electroacoust* 1967;15:70–73.
- Weng X, Cloutier G, Beaulieu R, Roederer G. Influence of acute-phase proteins on erythrocyte aggregation. *Am J Physiol Heart Circ Physiol* 1996a;271:H2346–H2352.
- Weng X, Cloutier G, Pibarot P, Durand LG. Comparison and simulation of different levels of erythrocyte aggregation with pig, horse, sheep, calf, and normal human blood. *Biorheology* 1996b;33:365–377.
- Wertheim M. Exact solution of the Percus–Yevick integral equation for hard spheres. *Phys Rev Lett* 1963;10:321–323.
- Yao LX, Zagzebski JA, Madsen EL. Backscatter coefficient measurements using a reference phantom to extract depth-dependent instrumentation factors. *Ultrason Imaging* 1990;12:58–70.
- Yu FT, Armstrong JK, Tripette J, Meiselman HJ, Cloutier G. A local increase in red blood cell aggregation can trigger deep vein thrombosis: Evidence based on quantitative cellular ultrasound imaging. *J Thromb Haemost* 2011;9:481–488.
- Yuan Y, Shung K. Ultrasonic backscatter from flowing whole blood: I. Dependence on shear rate and hematocrit. *J Acoust Soc Am* 1988a;84:52–58.
- Yuan Y, Shung K. Ultrasonic backscatter from flowing whole blood: II. Dependence on frequency and fibrinogen concentration. *J Acoust Soc Am* 1988b;84:1195–1200.
- Yuan Y, Shung K. Echoicity of whole blood. *J Ultrasound Med* 1989;8:425–434.